# Hypersonic Viscous Shock-Layer Solutions over Long Slender Bodies—Part II: Low Reynolds Number Flows

K. P. Lee* and R. N. Gupta†
*Scientific Research and Technology, Inc., Hampton, Virginia 23666-1325*
and
E. V. Zoby‡ and J. N. Moss‡
*NASA Langley Research Center, Hampton, Virginia 23665-5225*

**Results are obtained for the surface pressure, drag, heat-transfer, and skin-friction coefficients for hyperboloids and sphere cones. Body half angles from 5 to 22.5 deg are considered for various low-density flow conditions. Recently obtained surface-slip and shock-slip equations are employed to account for the low-density effects. The method of solution employed for the visocus shock-layer (VSL) equations is a partially coupled, spatial-matching, implicit, finite-difference technique. The flow cases analyzed include highly cooled, long, slender bodies in high Mach number flows. The present perfect-gas VSL calculations compare quite well with available experimental data. Results have also been obtained from the steady-state, Navier-Stokes (NS) equations by successive approximations. A comparison between the NS and VSL results indicates that the VSL equations, even with body and shock-slip boundary conditions, may not be adequate in the stagnation region at altitudes greater than about 75 km for the cases of this investigation.**

## Nomenclature

$A^*$ = local cross-sectional area
$a_\infty^*$ = speed of sound in freestream
$C_D$ = total drag coefficient based on the local cross-sectional area, 2 drag/$(\rho_\infty^* U_\infty^{*2} A^*)$
$C_f$ = skin friction coefficient, $2\tau_w^*/(\rho_\infty^* U_\infty^{*2})$
$C_H$ = heat transfer coefficient, $2q^*/(\rho_\infty^* U_\infty^{*3})$
$C_p^*$ = specific heat at constant pressure
$C_p$ = pressure coefficient, $2p^*/(\rho_\infty U_\infty^{*2})$
$g$ = stretching function
$H$ = enthalpy, $H^*/U_\infty^{*2}$
$H^*$ = $h^* + (u^{*2}/2)$
$h$ = static enthalpy, $h^*/U_\infty^{*2}$
$K$ = thermal conductivity, $K^*/\mu_{\text{ref}}^* C_{p,\infty}^*$
$K^*$ = thermal conductivity
$Kn$ = freestream Knudsen number, $\lambda_\infty^*/R_N^*$
$M_\infty$ = freestream Mach number
$n$ = coordinate measured normal to the body, $n^*/R_N^*$
$Pr$ = Prandtl number, $C_p^*\mu^*/K^*$
$p$ = pressure, $p^*/(\rho_\infty^* U_\infty^{*2})$
$q$ = heat flux, $q^*/(\rho_\infty^* U_\infty^{*3})$
$R^*$ = universal gas constant, $R^* = 8.3143$ J/mol K
$R_N^*$ = body nose radius
$r$ = radius measured from axis of symmetry to a point on the body surface, $r^*/R_N^*$
$Re_\infty$ = freestream Reynolds number, $\rho_\infty^* U_\infty^* R_N^*/\mu_\infty^*$
$St$ = Stanton number, $-q/(H_\infty - H_w)$
$S_\infty$ = speed ratio, $U_\infty^*\sqrt{W^*/2R^*T_\infty^*}$
$s$ = coordinate measured along the body surface, $s^*/R_N^*$
$T$ = temperature, $T^*/T_{\text{ref}}^*$
$T_{0\infty}^*$ = freestream adiabatic stagnation temperature
$T_{\text{ref}}^*$ = $U_\infty^{*2}/C_{p,\infty}^*$
$U_\infty^*$ = freestream velocity
$u$ = velocity component tangent to body surface, $u^*/U_\infty^*$
$v$ = velocity component normal to body surface, $v^*/U_\infty^*$
$W^*$ = molecular weight
$\alpha$ = shock angle defined in Fig. 1
$\bar{\alpha}$ = mesh refinement parameter
$\alpha_1, \alpha_2, \alpha_3, \alpha_4$ = coefficients in Eq. (1)
$\beta$ = angle defined in Fig. 1
$\bar{\beta}$ = mesh refinement parameter
$\gamma$ = ratio of specific heats
$\epsilon$ = Reynolds number parameter, $\epsilon = [\mu_{\text{ref}}^*/\rho_\infty^* U_\infty^* R_N^*]^{1/2}$
$\bar{\eta}$ = transformed $\eta$ coordinate, $n/n_{sh}$
$\eta$ = transformed $\bar{\eta}$ coordinate, $g(\bar{\eta})$
$\Delta\bar{\eta}_1$ = stepsize adjacent to the surface
$\theta$ = body angle defined in Fig. 1
$\bar{\theta}$ = accommodation coefficient
$\kappa$ = body curvature, $\kappa^* R_N^*$
$\lambda_\infty^*$ = freestream mean-free path
$\mu$ = viscosity, $\mu^*/\mu_{\text{ref}}^*$
$\mu_{\text{ref}}^*$ = reference viscosity, $\mu^*(T_{\text{ref}}^*)$
$\xi$ = coordinate measured along the body surface, $\xi = s$
$\rho$ = density, $\rho^*/\rho_\infty^*$
$\tau$ = shear stress, $\tau^*/(\rho_\infty^* U_\infty^{*2})$

Presented as Paper 88-0460 at the AIAA 26th Aerospace Sciences Meeting, Reno, NV, Jan. 11-14, 1988; received June 26, 1989; revision received Sept. 5, 1989. 

*Research Engineer. Member AIAA.
†President. Associate Fellow AIAA.
‡Research Engineer, Aerothermodynamics Branch. Associate Fellow AIAA.

*Subscripts*

| | |
|---|---|
| *aw* | = adiabatic wall |
| *s* | = value at edge of Knudsen layer |
| *sh* | = shock value |
| *w* | = wall value |
| ∞ | = freestream value |

*Superscripts*

| | |
|---|---|
| *j* | = zero for plane flow and one for axisymmetric flow |
| ~ | = shock oriented velocity components |
| ′ | = total differential |
| * | = dimensional quantity |

## Introduction

FLOW conditions encountered by transatmospheric flight vehicles[1,2] require an understanding of the flowfield-vehicle interactions over a wide range of Reynolds numbers. High Reynolds number solutions[3] are needed at low-altitude flight conditions; whereas low Reynolds number (or low-density) solutions are desired at the higher altitudes. The low-density flows are important to understand since some missions require maneuvers at these conditions, and vehicle aerodynamics could be influenced significantly. Under the low Reynolds number flow conditions, the viscous effects influence almost the entire shock layer, and the shock itself is considerably thick compared to the high Reynolds numbers case. These low-density effects require the use of a more comprehensive set of governing equations than the classical boundary-layer equations. The complete Navier-Stokes equations are considered[4] appropriate for low Reynolds number applications. Nevertheless, solutions based on these equations are very expensive due to large computer run time and storage requirements. The viscous shock-layer (VSL) equations[5] represent an intermediate level of approximation between the boundary-layer and Navier-Stokes equations. The VSL equations are obtained from the Navier-Stokes equations by retaining terms up to second order in the inverse square root of the Reynolds number from both the viscous and the inviscid regions of the flow. This results in a simplified set of governing equations that are uniformly valid through the shock layer to moderately low Reynolds numbers. The body surface conditions are given by slip and temperature jump conditions[6]; whereas a set of shock slip conditions[5] are used to determine conditions behind the shock. Slip at the body surface is a second-order effect, which is the same as the order of approximation involved in obtaining the VSL equations. Shock slip is a third-order effect and is, therefore, of higher order than the body slip.

The surface-slip conditions obtained by Davis[5] have been corrected[6] recently. Further, the shock-slip boundary condition of Ref. 5 contained derivatives of the shock quantities in the body-oriented coordinate system instead of the shock-oriented coordinate system. This introduces errors in analyzing flows past slender bodies. The reader is cautioned about the possible adverse effect these errors may have on results presented in existing analyses.[7-9]

The noncontinuum methods such as the direct simulation Monte Carlo[10] (DSMC) are considered more appropriate for the calculation of low-density flows. However, large computer resources are required by the DSMC method as compared to a continuum method such as the VSL method. The recent work of Ref. 4 shows that the continuum prediction techniques can give good results for the low-density flows if proper accounting is made of the high-altitude effects.

In the present work, a recently developed VSL code[3] has been used to obtain results for the low-density flight conditions for long, slender bodies. The surface-slip[6] and the currently corrected shock-slip boundary conditions are implemented in this study for a perfect gas. A detailed comparison of the present results with experiments and other predictions gives an estimate of accuracy of the current VSL predictions. Further, the range of applicability of the VSL solutions is ascertained by comparing these with those obtained from the steady-state, Navier-Stokes (NS) equations.

## Analysis

### Flow Governing Equations

The conservation equations employed in the present analysis are the steady-perfect-gas, viscous, shock-layer equations[5] for an axisymmetric or two-dimensional body at zero angle of attack (see Fig. 1 of Part I of this study). (The steady-state form of the NS equations is taken from Ref. 11. For the NS equations, coefficient $\alpha_3$ given by Eqs. (2c) and (3c) and the normal momentum equation, Eq. (5), given in Part I of this study are modified as given in Appendix A.) These equations in the orthogonal, body-oriented, transformed coordinates are provided as Eqs. (1-6) in Part I of this study and may be obtained from there by specifying the eddy viscosity $\epsilon^+$ as zero. Transformation equations given as Eqs. (7a-7e) in Part I refine the mesh near the body and shock equally in the physical plane with $\bar{\alpha} = \frac{1}{2}$ and give a uniform mesh in the computational coordinate $\eta$.

### Boundary Conditions

The following wall and shock-boundary conditions are employed.

**Surface Conditions**[6]

Velocity slip

$$u_s = \sqrt{\frac{\pi}{2}}\left(\frac{2-\bar{\theta}}{\bar{\theta}}\right)\frac{\epsilon^2\mu_s}{\sqrt{p_s\rho_s}}\left[\frac{1}{n_{sh}}\frac{\partial g}{\partial\bar{\eta}}\frac{\partial u}{\partial\eta} - \frac{\kappa u}{(1+\bar{\eta}n_{sh}\kappa)}\right]_s \tag{1a}$$

Pressure slip

$$p_s = p_w + \frac{4}{5\sqrt{2\pi}}\left(\frac{\gamma}{\gamma-1}\right)\left(\frac{2-\bar{\theta}}{\bar{\theta}}\right)\frac{\epsilon^2}{Pr}\frac{\mu_s}{T_s}\frac{\sqrt{p_s}}{\sqrt{\rho_s}}\left(\frac{1}{n_{sh}}\frac{\partial g}{\partial\bar{\eta}}\frac{\partial T}{\partial\eta}\right)_s \tag{1b}$$

Temperature jump

$$T_s = T_w + \frac{1}{2}\sqrt{\frac{\pi}{2}}\left(\frac{\gamma}{\gamma-1}\right)\left(\frac{2-\bar{\theta}}{\bar{\theta}}\right)\frac{\epsilon^2}{Pr}\frac{\mu_s}{\sqrt{p_s\rho_s}}\left(\frac{1}{n_{sh}}\frac{\partial g}{\partial\bar{\eta}}\frac{\partial T}{\partial\eta}\right)_s \tag{1c}$$

**Shock Conditions** (corrected form of Ref. 5)

Continuity

$$\rho_{sh}\tilde{v}_{sh} = -\sin\alpha \tag{2a}$$

$s$-Momentum

$$\epsilon^2\mu_{sh}\left\{\underline{\left[\cos(\alpha-\theta)+\bar{\eta}\frac{\partial n_{sh}}{\partial\xi}\sin(\alpha-\theta)\right]\frac{1}{n}\frac{\partial g}{\partial\bar{\eta}}\frac{\partial\tilde{u}}{\partial\eta}} - \underline{\frac{\partial\tilde{u}}{\partial\xi}\sin(\alpha-\theta)}\right\}_{sh} + \tilde{u}_{sh}\sin\alpha = \sin\alpha\cos\alpha \tag{2b}$$

$n$-Momentum

$$p_{sh} = p_\infty + \sin\alpha(\sin\alpha + \tilde{v}_{sh}) \tag{2c}$$

Energy

$$\epsilon^2\left(\frac{\mu}{Pr}\right)_{sh}\left\{\underline{\left[\cos(\alpha-\theta)+\bar{\eta}\frac{\partial n_{sh}}{\partial\xi}\sin(\alpha-\theta)\right]\frac{1}{n}\frac{\partial g}{\partial\bar{\eta}}\frac{\partial T}{\partial\eta}} - \underline{\frac{\partial T}{\partial\xi}\sin(\alpha-\theta)}\right\}_{sh} + T_{sh}\sin\alpha$$
$$-\frac{\sin\alpha}{2}(\tilde{u}_{sh}-\cos\alpha)^2 = \frac{\sin\alpha}{2}\left\{\frac{4\gamma}{(\gamma+1)^2}\sin^2\alpha + \left[\left(\frac{2}{\gamma-1}\right)-\frac{4(\gamma-1)}{(\gamma+1)^2}\right]\frac{1}{M_\infty^2} - \frac{4}{(\gamma+1)^2M_\infty^4\sin^2\alpha}\right\} \tag{2d}$$

Equation of State

$$\rho_{sh} = \gamma p_{sh}/(\gamma - 1)T_{sh} \tag{2e}$$

In Eqs. (2a-2e), $\tilde{u}$ and $\tilde{v}$ are the components of velocity tangent and normal to the shock interface, respectively, and are related to the components in the body-oriented coordinates as

$$\tilde{u}_{sh} = u_{sh}\cos(\alpha - \theta) + v_{sh}\sin(\alpha - \theta) \tag{2f}$$

$$\tilde{v}_{sh} = -u_{sh}\sin(\alpha - \theta) + v_{sh}\cos(\alpha - \theta) \tag{2g}$$

There are errors in the expressions for surface pressure and temperature slip [i.e., Eqs. (2.7c) and (2.7d)] of Ref. 5. The pressure and temperature slip values are underpredicted there by the ratio of $K/\mu$ as explained in Ref. 6. For a perfect gas, this ratio is the same as $1/Pr$. Similarly, Eqs. (2.8d) and (2.8e) of Ref. 5, for the tangential velocity and temperature slip at the shock, contain normal derivatives of the shock quantities in the body-oriented coordinate system in place of the shock-oriented coordinates as given by the underlined terms in Eqs. (2b) and (2d).

For ease in numerical computations, the governing equations given in Part I, as well as the boundary conditions provided here, are further transformed by normalizing most of the dependent variables with their local shock values. An exception is that the normal velocity $v$ is not normalized because it may not be well behaved. This occurs because the $v$-component of velocity may either experience a change of direction or be near zero at the shock.

## Method of Solution

Some of the early VSL calculations were carried out in Ref. 5 for moderate Reynolds number flow conditions. In Ref. 5, the governing equations are solved in a successive manner where an approximate initial shock shape is required to make the VSL equations (which are weakly elliptic in the tangential direction) parabolic. This procedure allows the use of a numerical scheme with space marching in the streamwise direction. In the approach of Ref. 5, the initial shock shape is obtained from the thin-shock-layer approximation; whereas in Ref. 8, the shock is obtained from an inviscid solution. Both of these approaches may not be feasible for the low-density conditions over a slender body. In addition, it is not clear from Ref. 8 if more than one global pass has been used to obtain the results. In the present method of solution, the initial shock shape is obtained from the corresponding cone angle solution at a high Reynolds number.[3] For a very low Reynolds number, the initial shock shape may be obtained by reducing the Reynolds number sequentially by a factor of 10 or so. This approach gives a very good estimate of the initial shock shape and results in a consistent convergence of the solutions. An alternate method,[12] which avoids the prescription of the initial shock shape, has recently been suggested for the high-density flows. However, this method may not be computationally efficient for long, slender bodies. Moreover, for faster convergence and stability, a good initial shock shape is desirable for this method also. In the present approach, the continuity and normal momentum equations are solved simultaneously as a coupled set (similar to that in Ref. 13) to overcome the stability problems encountered in the method of Ref. 5 for slender bodies. The tangential momentum and energy equations are still solved in a successive manner. Details of the method of solution (which is an implicit finite-difference method) are given in Ref. 3, and, therefore, it will only be briefly described here.

Let the subscript $m$ denote the station measured along the body surface and $n$ denote the station measured normal to the body surface. The second-order $s$-momentum and energy equations are replaced with central differences taken in the $\eta$-direction and two-point backward differences in the $\xi$-direction at the point $(m,n)$. Further, based on the hypersonic small disturbance theory for a slender body and the procedure of Ref. 13, the first-order global continuity equation and $n$-momentum equation are solved for the pressure $p$ and normal velocity $v$ in a coupled way. The density in these equations is eliminated through the use of the equation of state. The continuity and normal momentum equations are expressed in finite-difference form at points $(m, n+\frac{1}{2})$ and $(m, n-\frac{1}{2})$ using a box scheme discussed by Richtmyer and Morton.[14] In these two coupled equations, $p$ and $v$ are eliminated alternatively to solve for these two variables.

The solution is started at the stagnation point where the various flowfield quantities are expanded[4,15] in terms of the distance $\xi$ along the body surface. These series expansions reduce the governing partial differential equations to ordinary differential equations in terms of $\eta$. At a body location $m$, other than the stagnation point, a two-point backward difference is used for the derivative with respect to $\xi$ at the point $(m,n)$ as mentioned earlier. This again gives ordinary differential equations at location $m$ in terms of $\eta$ for the $s$-momentum and energy equations. The finite-difference form of these equations can be solved by using the Thomas algorithm. The coupled equations for $p$ and $v$ are solved by using a box scheme mentioned previously.

The Vigneron condition[16] is used for the pressure gradient in the streamwise momentum equation in the subsonic nose region. In this condition, a portion of the pressure gradient is treated implicitly by employing a two-point backward difference. The remaining portion of the pressure gradient is forward differenced to allow for upstream influences. The global iterations are employed in the subsonic region to update the pressure (and shock shape). In the supersonic flow region, the full pressure-gradient term is employed with a two-point backward difference. For small shock-slip values, global iterations may not be required in this region.

Solutions to the steady-state, NS equations[17] have been obtained by first expressing them in the body-oriented coordinate system. Next, by employing a solution of the VSL equations by the method briefly described earlier, the higher-order NS terms (Appendix A) are evaluated. These terms are held constant during the solution for the first approximation to the NS equations. The solution with this approximation is obtained at the end of first global pass. At the beginning of second global pass, the higher-order terms are re-evaluated from the first approximation solutions. These terms are held constant again during the solution for the second approximation obtained at the end of the second global pass. This procedure is repeated until the flowfield results corresponding to successive global passes converge within a specified limit. A method similar to the present was also employed in Ref. 18.

## Discussion of Results

Numerical solutions of the VSL equations for the low-density hypersonic flow over long slender bodies are obtained. The surface slip[6] and the recently corrected shock-slip boundary conditions are implemented in the implicit finite-difference method used to solve the governing equations. Detailed comparisons with the experimental data are included for several conditions. The effects of grid spacing, body angle, and surface temperature on the low-density calculations are also demonstrated. The surface temperature conditions range from adiabatic to highly cooled and the results are computed for various altitude conditions at $M_\infty = 20$. Calculations from the steady-state, NS equations are also provided to indicate the range of applicability of VSL solutions.

### Comparison with Experimental Data

There are only a few experimental data for the low-density, high-energy flows available in the literature. The data of Little[19] provide measurements of pressure, drag, and skin friction and are still considered quite good for such flows. The drag coefficient data measured over a 10-deg hyperboloid at

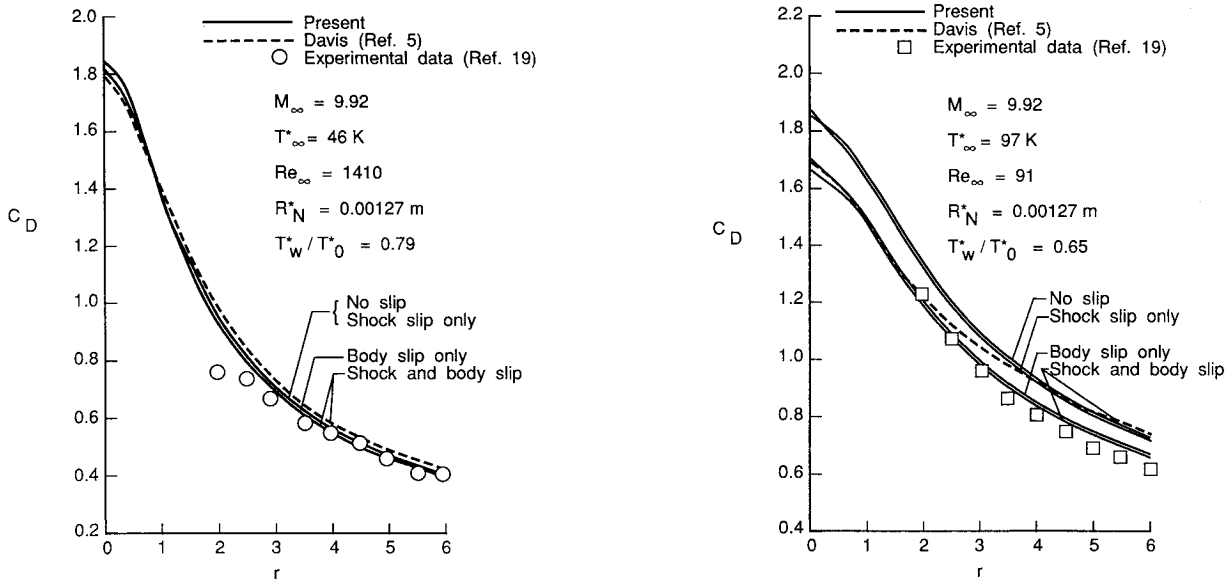


**Fig. 1 Drag coefficient for a 10-deg hyperboloid from VSL method.**

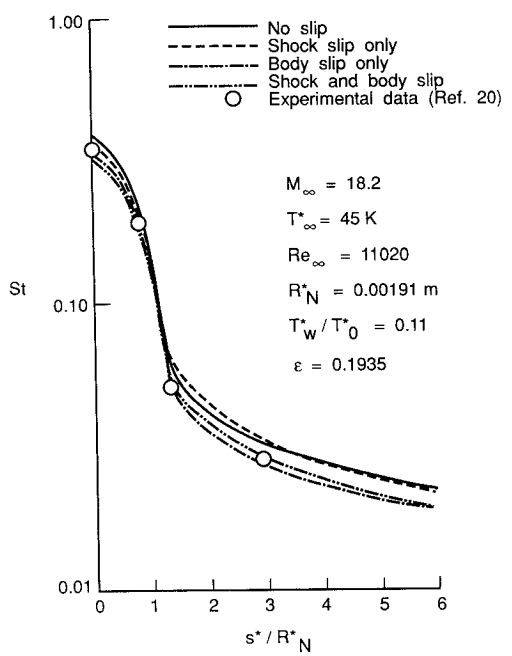


**Fig. 2 Stanton number distribution for a 10-deg sphere cone from VSL method.**

Mach numbers of 9.92 and 9.2 are presented in Figs. 1a and 1b, respectively, and are compared with results of the present method and those of Ref. 5. Clearly the drag coefficient predictions by the present method with shock and body slip are in much better agreement with the experimental data than the predictions of Ref. 5 for a range of values of the rarefaction parameter $\epsilon$. Large differences in the present calculations and those of Ref. 5 are seen with the increasing values of $\epsilon$. Note that the effect of including shock slip is insignificant for these conditions.

Surface heat-transfer data at low Reynolds number conditions are obtained from Ref. 20. These data in the form of a Stanton number were measured over a 10-deg sphere cone at a Mach number of 18.2 and are presented in Fig. 2. The present calculations with shock and body slip are in good agreement with the data of Ref. 20 except for the stagnation point where the data are considered to be biased upward[21] resulting from the particle impact caused by the arc heater.

### Comparison with Predicted Results

The present results obtained from the VSL and steady-state NS equations are compared in Table 1 with those obtained by Anderson and Moss.[18] The results from these calculations compare fairly well, especially for $C_p$. A maximum difference of less than about 10% occurs between the two results at $Re_\infty$ of 90 in the heat transfer coefficient $C_H$. This discrepancy may

**Table 1 VSL and NS calculations in the stagnation region of a 22.5-deg hyperboloid**

| | | | | | Present | | | | | | Anderson and Moss[18] | | | |
|---|---|---|---|---|---|---|---|---|---|---|---|---|---|---|
| | | | | | VSL no slip | | VSL body and shock slip | | NS body and shock slip | | VSL body and shock slip | | NS body and shock slip | |
| $Re_\infty$ | $T_W/T_0$ | $T_\infty, R$ | $\epsilon$ | $M_\infty$ | $C_H$ | $C_p$ | $C_H$ | $C_p$ | $C_H$ | $C_p$ | $C_H$ | $C_p$ | $C_H$ | $C_p$ |
| 31160 | 0.08 | 474 | 0.024 | 19.10 | 0.037 | 1.84 | 0.037 | 1.74 | 0.037 | 1.74 | — | 1.77 | — | 1.80 |
| 1035 | 0.79 | 83 | 0.140 | 9.92 | 0.039 | 1.85 | 0.036 | 1.82 | 0.039 | 1.85 | — | 1.82 | — | 1.87 |
| 90 | 0.65 | 174 | 0.366 | 9.20 | 0.281 | 1.86 | 0.158 | 1.72 | 0.208 | 1.99 | 0.169 | 1.74 | 0.225 | 2.00 |

be due to the refined grid clustering employed near the shock and body in the present calculations.

### Effects of Grid Spacing, Body Angle, Altitude, and Surface Temperature

Predicted skin-friction distributions based on the present method and that of Ref. 12 are presented in Fig. 3. The comparison between the present values and those of Ref. 12 is quite good when the coarse grid structure of Ref. 12 is used. The method of Ref. 12 is fully coupled as compared to the coupling between the normal momentum and continuity equations only in the present method. The full coupling requires solving a $5 \times 5$ matrix at every point in the flowfield for a perfect gas. Also, the computational times should be very large for long, slender bodies with this method. Therefore, the present approach may be more appealing for such flow conditions. Figure 3 also presents results with and without slip for a more refined grid near the shock and body surface. These results are shown to be higher than the course grid calculations. Clearly, the computational grid-size as well as the slip effects are demonstrated to be important at these flow conditions.

The effect of cone angle with surface and shock-slip boundary conditions is illustrated in the results presented in Figs. 4 and 5. The flow analyzed in these figures is at a freestream Mach number of 20 over 5- and 10-deg cones, respectively, for a highly cooled surface ($T_w = 300$ K) and a small nose radius ($R_N = 2.54$ cm). The results are presented in terms of the Stanton number for different body locations as a function of the rarefaction parameter $\epsilon$ or altitude. The slip effects become insignificant for both cone angles at body locations greater than about 90 nose radii or at altitudes less than about 60 km for the flow in the nose region. The largest slip effects are shown to occur in the nose region. Figures 4 and 5 also indicate that, for a given altitude and body location, the slip effects are higher on the conical flank portion for a 5-deg sphere cone than for a 10-deg sphere cone. Further, the effect of slip increases with the increase in altitude for a given cone angle and body location.

Figures 6 and 7 illustrate the effect of surface temperature on stagnation-point pressure and heat-transfer coefficients, respectively. Both VSL and NS calculations are provided in these two figures. In Figs. 6a and 6b, the VSL results for $C_p$ with no slip gradually increase from a value of 1.84 at about 30.5 km altitude to a value of 1.88 at 100 km altitude. The Reynolds number parameter $\epsilon$ ranges from 0.01 to $\sim 1$ for this altitude range. The value of $C_p$ stays constant at 1.84 for an adiabatic wall. The VSL predictions for $C_p$ with slip continuously decrease with increasing altitude for a cooled surface. This trend is similar to the one given by the results of Ref. 5. This trend, however, indicates that the VSL results with slip do not approach the free molecular value (see Appendix B) at higher altitudes. The NS results with body and shock slip do provide the right behavior of approaching the free-molecular

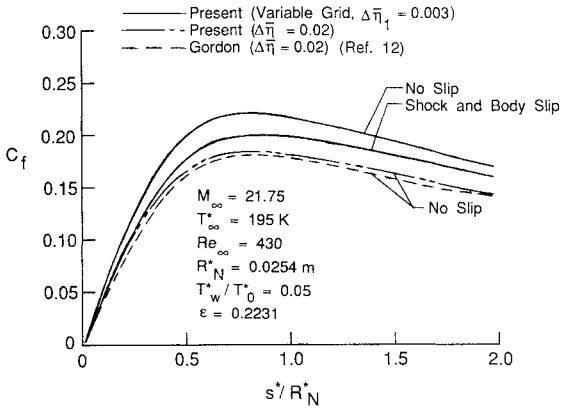


**Fig. 3 Skin-friction coefficient distribution for a 22.5-deg hyperboloid from VSL method.**

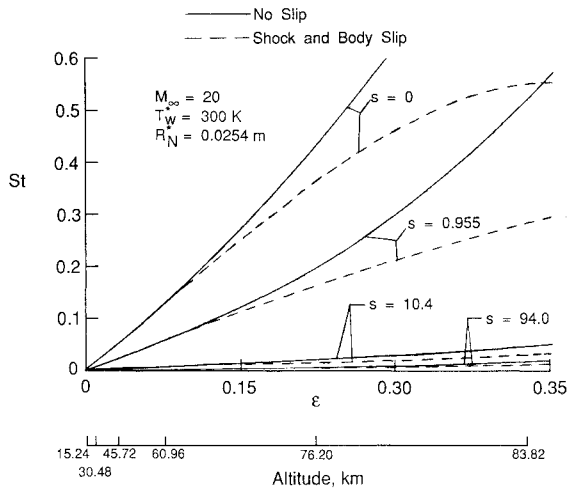


**Fig. 4 Stanton number distribution for a 5-deg sphere cone from VSL method.**

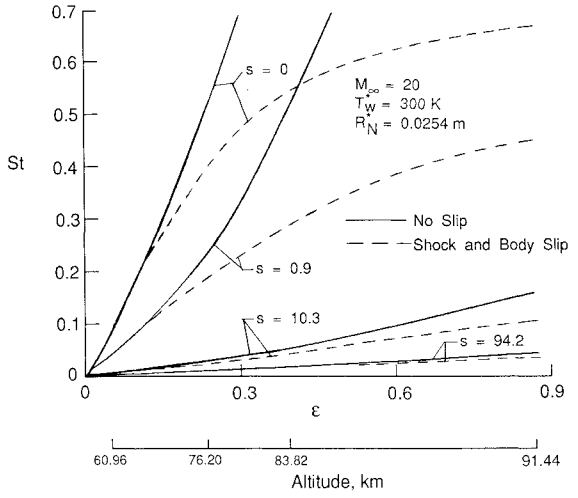


**Fig. 5 Stanton number distribution for a 10-deg sphere cone from VSL method.**

flow value at higher altitudes. These results, however, first show a decrease in the value of $C_p$ and then an increase as the altitude further increases. This behavior is consistent with the results obtained in Ref. 22 and is similar to the trend observed by Potter and Bailey.[23] A good agreement between the NS results and the data of Ref. 23 was reported in Ref. 22. As can be noticed from Figs. 6a and 6b, the dip in the pressure coefficient curve is reduced by increasing the wall temperature. For an adiabatic surface (implying no temperature slip), there is no such effect on the $C_p$ curve, which increases monotonically toward the free-molecular flow value with increasing altitude. Note that the free-molecular flow value of $C_p$ as well as its asymptotic value at lower altitudes is also influenced by the wall temperature. The free-molecular flow value is obtained from the equations of Ref. 24. The predicted value of $C_p$ from NS and VSL solutions with slip approaches the asymptotic value of 1.84 at lower altitudes with the increase in surface temperature, which is the value predicted by the inviscid modified Newtonian formulation. Obviously, this value is obtained for a very high Reynolds number flow in absence of any slip effects. Reducing the slip effects by increasing the wall temperature also gives this asymptotic value at moderately high altitudes (Fig. 6b).

The stagnation-point heat-transfer coefficient vs freestream Knudsen number (or altitude) calculations for different surface temperatures are presented in Figs. 7a and 7b. Results for a given surface temperature show that VSL formulation with or without slip does not give physically realistic results at very

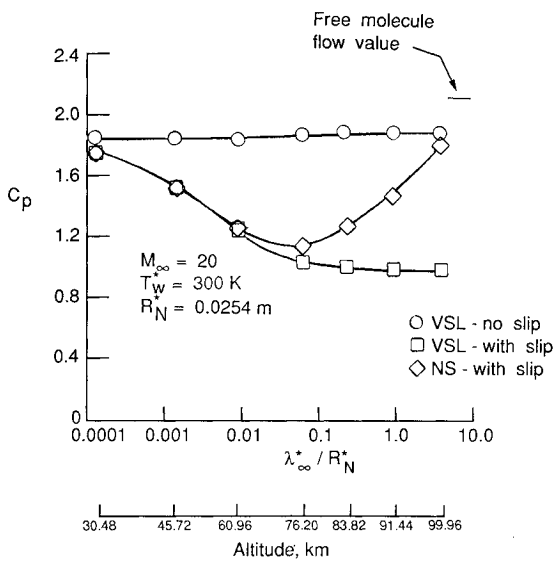


a) $T^*_w = 300$ K

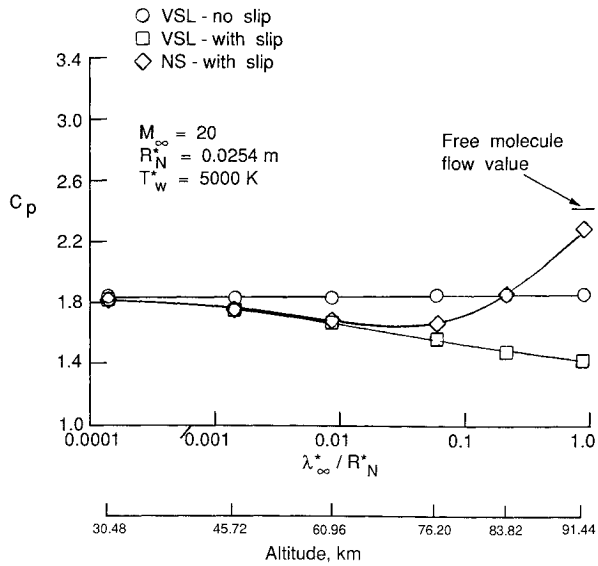


b) $T^*_w = 5000$ K

**Fig. 6 Stagnation-point pressure coefficient vs Knudsen number and altitude.**

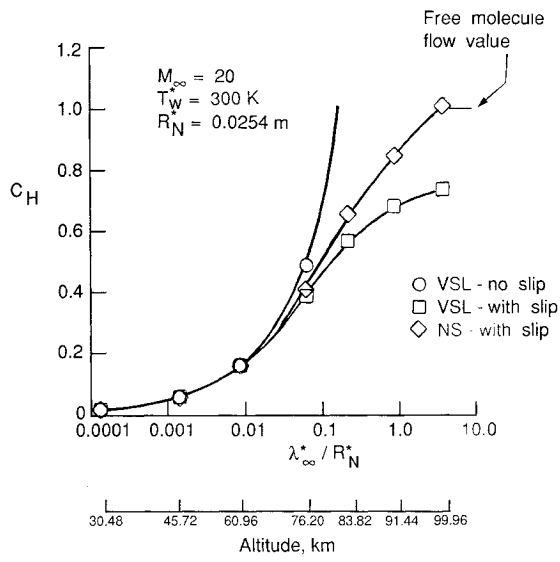


a) $T^*_w = 300$ K

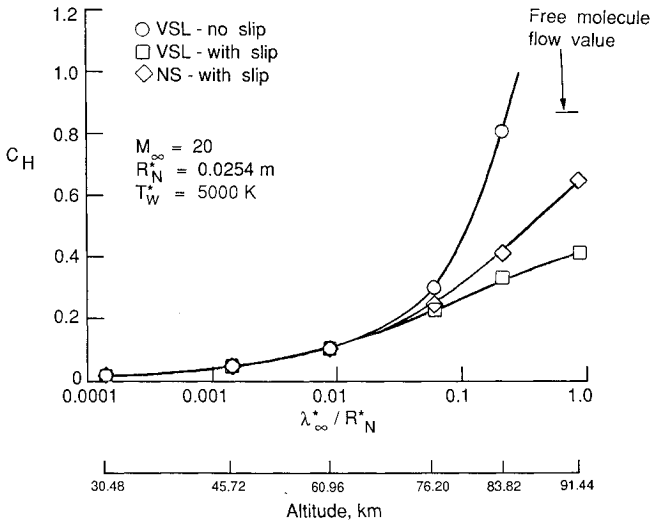


b) $T^*_w = 5000$ K

**Fig. 7 Stagnation-point, heat-transfer coefficient vs Knudsen number and altitude.**

high altitudes. The NS results with slip do approach the free-molecular flow value of approximately unity at very high altitudes. This perfect-gas result agrees with the NS analysis of Ref. 4 with finite-rate chemistry. With the increase in surface temperature, the surface heat-transfer rate is decreased as expected. The effect of slip is noticeable down to an altitude of about 60 km for the surface temperatures considered here. Discrepancies in results with and without slip of less than 10% are observed below approximately 75 km altitude.

Results of Figs. 6 and 7 suggest that the VSL calculations with slip begin to deviate from the NS results with slip for freestream Knudsen numbers ($\lambda^*_\infty/R^*_N$) greater than about 0.06. For $C_p$ the deviation begins at $\lambda^*_\infty/R^*_N \approx 0.01$). It may not be appropriate to use the VSL model even with body and shock slip at higher altitudes, especially for the stagnation region. Even the Navier-Stokes model may not be appropriate to use for Knudsen number values of much greater than unity. For higher values of the Knudsen number, computational methods of type Ref. 10 would be applicable.

## Conclusions

Results have been obtained for the surface pressure, drag, heat transfer, and skin-friction coefficients for slender-body hyperboloids and sphere cones under varying degrees of low-density flow conditions. Recently obtained surface-slip and corrected shock-slip conditions are employed to account for the low-density effects. The method of solution used for the viscous shock-layer (VSL) equations is a partially coupled spatial-marching implicit finite-difference technique. The flow cases analyzed include highly cooled surfaces in very high Mach number flows. The VSL predictions compare quite favorably with experimental data. Results are also obtained from the steady-state Navier-Stokes (NS) equations by successive approximations, using the VSL results to evaluate higher order terms for the first approximation. A comparison between the NS and VSL results indicates that the VSL equations, even with body and shock slip, do not give physically consistent results in the stagnation region above approximately 75-km altitude for the conditions considered in this study.

## Appendix A: Coefficient $\alpha_3$ for the Navier-Stokes Equations

For the steady-state NS equations, coefficient $\alpha_3$ appearing in Eq. (1) of Part I should be replaced by $\alpha_3'$, which is defined as

*s*-Momentum

$$\alpha_3' = \alpha_3 + \frac{n_{sh}^2}{\epsilon^2 \mu}(\mathrm{HOT})_s \tag{A1}$$

Energy equation

$$\alpha_3' = \alpha_3 + \frac{n_{sh}^2}{\epsilon^2(\mu/Pr)}[u(\mathrm{HOT})_s + (\mathrm{HOT})_e] \tag{A2}$$

where $\alpha_3$ in Eqs. (A1) and (A2) is given by Eqs. (2c) and (3c), respectively, of Part I. The abbreviation "HOT" in Eqs. (A1) and (A2) represents higher-order terms, and subscripts "*s*" and "*e*" imply terms in the *s*-momentum and energy equations.

The normal momentum equation, Eq. (5), given in Part I is modified for the NS model to

$$(\mathrm{LHS})_{\mathrm{Eq}(5)} - (\mathrm{HOT})_n = 0 \tag{A3}$$

where the first term in Eq. (A3) implies the entire left-hand side of Eq. (5) of Part I, and the second term represents the higher-order terms in the *n*-momentum equation.

The higher-order terms appearing in Eqs. (A1) through (A3) are defined as

$$\begin{aligned}(\mathrm{HOT})_s = {} & \frac{\epsilon^2}{(1+\bar\eta n_{sh}\kappa)}\left(\frac{\partial C_1}{\partial\xi} - \bar\eta\frac{n_{sh}'}{n_{sh}}\frac{\partial C_1}{\partial\eta}\frac{dg}{d\bar\eta}\right) \\ & - \frac{\epsilon^2}{(1+\bar\eta n_{sh}\kappa)}\left(\frac{\partial C_2}{\partial\xi} - \bar\eta\frac{n_{sh}'}{n_{sh}}\frac{\partial C_2}{\partial\eta}\frac{dg}{d\bar\eta}\right) + \frac{\epsilon^2}{n_{sh}}\frac{\partial C_3}{\partial\eta}\frac{dg}{d\bar\eta} \\ & + \frac{\epsilon^2\mu}{(1+\bar\eta n_{sh}\kappa)} \times \left(\frac{2\kappa}{1+\bar\eta n_{sh}\kappa} + \frac{\cos\theta}{r+\bar\eta n_{sh}\cos\theta}\right) \\ & \times \left(\frac{\partial v}{\partial\xi} - \bar\eta\frac{n_{sh}'}{n_{sh}}\frac{\partial v}{\partial\eta}\frac{dg}{d\bar\eta}\right) + \frac{2\epsilon^2\mu}{(1+\bar\eta n_{sh}\kappa)(r+\bar\eta n_{sh}\cos\theta)} \\ & \times \left[\frac{\partial(r+\bar\eta n_{sh}\cos\theta)}{\partial\xi} - \bar\eta n_{sh}'\cos\theta\right] \\ & \times \left\{\frac{1}{(1+\bar\eta n_{sh}\kappa)}\left[\frac{\partial u}{\partial\xi} - \bar\eta\frac{n_{sh}'}{n_{sh}}\frac{\partial u}{\partial\eta}\frac{dg}{d\bar\eta}\right]\right. \\ & - \frac{u}{(1+\bar\eta n_{sh}\kappa)(r+\bar\eta n_{sh}\cos\theta)} \\ & \times \left[\frac{\partial(r+\bar\eta n_{sh}\cos\theta)}{\partial\xi} - \bar\eta n_{sh}'\cos\theta\right] \\ & \left. + v\left[\frac{\kappa}{1+\bar\eta n_{sh}\kappa} - \frac{\cos\theta}{r+\bar\eta n_{sh}\cos\theta}\right]\right\} \end{aligned} \tag{A4}$$

$$\begin{aligned}(\mathrm{HOT})_n = {} & \frac{\epsilon^2}{(1+\bar\eta n_{sh}\kappa)}\left[\frac{\partial C_4}{\partial\xi} - \bar\eta\frac{n_{sh}'}{n_{sh}}\frac{\partial C_4}{\partial\eta}\frac{dg}{d\bar\eta}\right] \\ & + \frac{\epsilon^2 C_4}{(1+\bar\eta n_{sh}\kappa)(r+\bar\eta n_{sh}\cos\theta)} \\ & \times \left[\frac{\partial(r+\bar\eta n_{sh}\cos\theta)}{\partial\xi} - \bar\eta n_{sh}'\cos\theta\right] + \frac{\epsilon^2}{n_{sh}}\frac{\partial C_5}{\partial\eta}\frac{dg}{d\bar\eta} \\ & - \frac{\epsilon^2}{n_{sh}}\frac{\partial C_6}{\partial\eta}\frac{dg}{d\bar\eta} + \frac{\epsilon^2\kappa C_9}{1+\bar\eta n_{sh}\kappa} + \frac{\epsilon^2 C_{10}\cos\theta}{r+\bar\eta n_{sh}\cos\theta} \end{aligned} \tag{A5}$$

$$\begin{aligned}(\mathrm{HOT})_e = {} & \frac{\epsilon^2}{(1+\bar\eta n_{sh}\kappa)(r+\bar\eta n_{sh}\cos\theta)}\left[\frac{\partial C_7}{\partial\xi} - \bar\eta\frac{n_{sh}'}{n_{sh}}\frac{\partial C_7}{\partial\eta}\frac{dg}{d\bar\eta}\right] \\ & - \frac{\epsilon^2}{(1+\bar\eta n_{sh}\kappa)(r+\bar\eta n_{sh}\cos\theta)}\left[\frac{\partial C_8}{\partial\xi} - \bar\eta\frac{n_{sh}'}{n_{sh}}\frac{\partial C_8}{\partial\eta}\frac{dg}{d\bar\eta}\right] \\ & + \frac{9}{8}\frac{\epsilon^2 C_1^2}{\mu} + 2\epsilon^2\mu\left[\frac{1}{n_{sh}}\frac{\partial v}{\partial\eta}\frac{dg}{d\bar\eta}\right]^2 \\ & + 2\epsilon^2\mu\left\{\frac{u}{(1+\bar\eta n_{sh}\kappa)(r+\bar\eta n_{sh}\cos\theta)}\right. \\ & \times \left[\frac{\partial(r+\bar\eta n_{sh}\cos\theta)}{\partial\xi} - \bar\eta n_{sh}'\cos\theta\right] + \left.\frac{v\cos\theta}{(r+\bar\eta n_{sh}\cos\theta)}\right\}^2 \\ & + \epsilon^2\mu\left\{\left[\frac{1}{(1+\bar\eta n_{sh}\kappa)}\left(\frac{\partial v}{\partial\xi} - \bar\eta\frac{n_{sh}'}{n_{sh}}\frac{\partial v}{\partial\eta}\frac{dg}{d\bar\eta}\right)\right]^2\right. \\ & + \frac{2}{(1+\bar\eta n_{sh}\kappa)} \times \left(\frac{\partial v}{\partial\xi} - \bar\eta\frac{n_{sh}'}{n_{sh}}\frac{\partial v}{\partial\eta}\frac{dg}{d\bar\eta}\right) \\ & \times \left.\left(\frac{1}{n_{sh}}\frac{\partial u}{\partial\eta}\frac{dg}{d\bar\eta} - \frac{u\kappa}{1+\bar\eta n_{sh}\kappa}\right)\right\} - \epsilon^2 C_{11} \end{aligned} \tag{A6}$$

Variables $C1$–$C11$ appearing in Eqs. (A4–A6) are given by

$$C_1 = \frac{4}{3}\mu\left\{\frac{1}{(1+\bar\eta n_{sh}\kappa)}\left[\frac{\partial u}{\partial\xi} - \bar\eta\frac{n_{sh}'}{n_{sh}}\frac{\partial u}{\partial\eta}\frac{dg}{d\bar\eta}\right] + \frac{v\kappa}{(1+\bar\eta n_{sh}\kappa)}\right\} \tag{A7}$$

$$\begin{aligned} C_2 = {} & \frac{2}{3}\mu\left\{\frac{1}{n_{sh}}\frac{\partial v}{\partial\eta}\frac{dg}{d\bar\eta} + \frac{v\cos\theta}{r+\bar\eta n_{sh}\cos\theta}\right. \\ & + \frac{u}{(1+\bar\eta n_{sh}\kappa)(r+\bar\eta n_{sh}\cos\theta)} \\ & \times \left.\left[\frac{\partial(r+\bar\eta n_{sh}\cos\theta)}{\partial\xi} - \bar\eta n_{sh}'\cos\theta\right]\right\} \end{aligned} \tag{A8}$$

$$C_3 = \frac{\mu}{(1+\bar\eta n_{sh}\kappa)}\left[\frac{\partial v}{\partial\xi} - \bar\eta\frac{n_{sh}'}{n_{sh}}\frac{\partial v}{\partial\eta}\frac{dg}{d\bar\eta}\right] \tag{A9}$$

$$\begin{aligned} C_4 = {} & \mu\left\{\frac{1}{(1+\bar\eta n_{sh}\kappa)}\left[\frac{\partial v}{\partial\xi} - \bar\eta\frac{n_{sh}'}{n_{sh}}\frac{\partial v}{\partial\eta}\frac{dg}{d\bar\eta}\right]\right. \\ & \left. + \frac{1}{n_{sh}}\frac{\partial u}{\partial\eta}\frac{dg}{d\bar\eta} - \frac{u\kappa}{1+\bar\eta n_{sh}\kappa}\right\} \end{aligned} \tag{A10}$$

$$C_5 = \frac{4}{3}\frac{\mu}{n_{sh}}\frac{\partial v}{\partial\eta}\frac{dg}{d\bar\eta} \tag{A11}$$

$$C_6 = \frac{2}{3}\mu\left\{\frac{1}{(1+\bar{\eta}n_{sh}\kappa)}\left[\frac{\partial u}{\partial \xi} - \bar{\eta}\frac{n'_{sh}}{n_{sh}}\frac{\partial u}{\partial \eta}\frac{\mathrm{d}g}{\mathrm{d}\bar{\eta}}\right] + \left[\frac{u}{(1+\bar{\eta}n_{sh}\kappa)(r+\bar{\eta}n_{sh}\cos\theta)}\right] \times \left[\frac{\partial(r+\eta n_{sh}\cos\theta)}{\partial \xi} - \bar{\eta}n'_{sh}\cos\theta\right] + v\left(\frac{\kappa}{1+\bar{\eta}n_{sh}\kappa} + \frac{\cos\theta}{r+\bar{\eta}n_{sh}\cos\theta}\right)\right\} \tag{A12}$$

$$C_7 = \frac{\mu}{Pr}\left(\frac{r+\bar{\eta}n_{sh}\cos\theta}{1+\bar{\eta}n_{sh}\kappa}\right)\left(\frac{\partial H}{\partial \xi} - \bar{\eta}\frac{n'_{sh}}{n_{sh}}\frac{\partial H}{\partial \eta}\frac{\mathrm{d}g}{\mathrm{d}\bar{\eta}}\right) \tag{A13}$$

$$C_8 = \frac{\mu u}{Pr}\left(\frac{r+\bar{\eta}n_{sh}\cos\theta}{1+\bar{\eta}n_{sh}\kappa}\right)\left(\frac{\partial u}{\partial \xi} - \bar{\eta}\frac{n'_{sh}}{n_{sh}}\frac{\partial u}{\partial \eta}\frac{\mathrm{d}g}{\mathrm{d}\bar{\eta}}\right) \tag{A14}$$

$$C_9 = 2\mu\left\{\frac{1}{\bar{n}_{sh}}\frac{\partial v}{\partial \eta}\frac{\mathrm{d}g}{\mathrm{d}\bar{\eta}} - \frac{v\kappa}{(1+\bar{\eta}n_{sh}\kappa)} - \frac{1}{(1+\bar{\eta}n_{sh}\kappa)}\left[\frac{\partial u}{\partial \xi} - \bar{\eta}\frac{n'_{sh}}{n_{sh}}\frac{\partial u}{\partial \eta}\frac{\mathrm{d}g}{\mathrm{d}\bar{\eta}}\right]\right\} \tag{A15}$$

$$C_{10} = 2\mu\left\{\left[\frac{1}{n_{sh}}\frac{\partial v}{\partial \eta}\frac{\mathrm{d}g}{\mathrm{d}\bar{\eta}}\right] - \frac{v\cos\theta}{r+\bar{\eta}n_{sh}\cos\theta} - \frac{u}{(1+\bar{\eta}n_{sh}\kappa)(r+\bar{\eta}n_{sh}\cos\theta)} \times \left[\frac{\partial(r+\bar{\eta}n_{sh}\cos\theta)}{\partial \xi} - \bar{\eta}n'_{sh}\cos\theta\right]\right\} \tag{A16}$$

$$C_{11} = \frac{2}{3}\mu\left\{\frac{1}{(1+\bar{\eta}n_{sh}\kappa)}\left[\frac{\partial u}{\partial \xi} - \bar{\eta}\frac{n'_{sh}}{n_{sh}}\frac{\partial u}{\partial \eta}\frac{\mathrm{d}g}{\mathrm{d}\bar{\eta}}\right] + \left[\frac{u}{(1+\bar{\eta}n_{sh}\kappa)(r+\bar{\eta}n_{sh}\cos\theta)}\right] \times \left[\frac{\partial(r+\bar{\eta}n_{sh}\cos\theta)}{\partial \xi} - \bar{\eta}n'_{sh}\cos\theta\right] + \frac{1}{n_{sh}}\frac{\partial v}{\partial \eta}\frac{\mathrm{d}g}{\mathrm{d}\bar{\eta}} + v\left[\frac{\kappa}{1+\bar{\eta}n_{sh}\kappa} + \frac{\cos\theta}{r+\bar{\eta}n_{sh}\cos\theta}\right]\right\}^2 \tag{A17}$$

## Appendix B: Pressure and Heat-Transfer Coefficients for Free-Molecule Flow

The pressure coefficient is obtained from[24]

$$C_p = \frac{2_p^*}{\rho_\infty^* U_\infty^{*2}} = \frac{p^*}{S^{*2}p_\infty^*} = \frac{2\bar{\beta}_\infty^2 p^*}{S^{*2}\rho_\infty^*} = \frac{1}{S^{*2}}\left\{\frac{1}{\sqrt{\pi}}S^*\cos\beta + \frac{1}{2}\left(\frac{T_W^*}{T_\infty^*}\right)^{1/2}\right\}\exp(-S^{*2}\cos^2\beta) + \frac{1}{S^{*2}}\left\{\frac{1}{2} + S^{*2}\cos^2\beta + \frac{1}{2}\left(\frac{T_W^*}{T_\infty^*}\right)^{1/2}\sqrt{\pi}S^*\cos\beta\right\} \times \left\{1+\mathrm{erf}(S^*\cos\beta)\right\} \tag{B1}$$

and the heat-transfer coefficient is given by[24]

$$C_H = \frac{2q_W^*}{\rho_\infty^* U_\infty^{*3}} = \frac{2\bar{\beta}_\infty^3 q_W^*}{S^{*3}\rho_\infty^*} = \frac{1}{2\sqrt{\pi}S^{*3}}\left(\left\{S^{*2} + \frac{\gamma}{\gamma-1} - \frac{\gamma+1}{2(\gamma-1)}\frac{T_W^*}{T_\infty^*}\right\} \times \left[\exp(-S^{*2}\cos^2\beta) + \sqrt{\pi}S^*\cos\beta\{1+\mathrm{erf}(S^*\cos\beta)\}\right] - \frac{1}{2}\exp(-S^{*2}\cos^2\beta)\right) \tag{B2}$$

In Eqs. (B1) and (B2), fully diffuse reflection from the surface is assumed. In these equations, $\beta$ is the angle between the unit normal vector and the direction of freestream velocity $U_\infty$ as shown in Fig. 1 of Part I. Parameters $\bar{\beta}_\infty$ and $S^*$ are defined as

$$\bar{\beta}_\infty = \left(2\frac{R^*}{W_\infty^*}T_\infty^*\right)^{-1/2} \tag{B3}$$

$$S^* = U_\infty^*\bar{\beta}_\infty \tag{B4}$$

## References


[1]Williams, R. M., "National Aerospace Plane: Technology for America's Future," *Aerospace America,* Vol. 24, No. 11, Nov. 1986, pp. 18–22.

[2]Martin, J. A., et al., "Special Section—Orbit-On-Demand Vehicle," *Aerospace America,* Vol. 23, No. 2, Feb. 1985, pp. 46–48.

[3]Gupta, R. N., Lee, K. P., Moss, J. N., Zoby, E. V., and Tiwari, S. N., "Viscous Shock-Layer Analysis of Long Slender Bodies," AIAA Paper 87-2487, Aug. 1987.

[4]Gupta, R. N., and Simmonds, A. L., "Hypersonic Low-Density Solutions of the Navier-Stokes Equations with Chemical Nonequilibrium and Multicomponent Surface Slip," AIAA Paper 86-1349, June 1986.

[5]Davis, R. T., "Numerical Solution of the Hypersonic Viscous Shock Layer Equations," *AIAA Journal,* Vol. 8, No. 5, May 1970, pp. 843–851.

[6]Gupta, R. N., Scott, C. D., and Moss, J. N., "Slip-Boundary Equations for Multicomponent Nonequilibrium Air Flow," NASA TP 2452, Nov. 1985; also, *Thermal Design of Aeroassisted Orbital Transfer Vehicles,* Vol. 96, Progress in Astronautics and Aeronautics, edited by H. F. Nelson, AIAA, New York, 1985, pp. 465–490.

[7]Tree, I. K., Melson, N. D., and Lewis, C. H., "Low Reynolds Number Hypersonic Ionizing Viscous Shock-Layer Flows Over the Jovian Probe," AIAA Paper 79-1080, June 1979.

[8]Song, D. J., and Swaminathan, S., "High Altitude Effects on Three-Dimensional Nonequilibrium Viscous Shock-Layer Flows," *Journal of Spacecraft and Rockets,* Vol. 22, No. 6, Nov.–Dec. 1985, pp. 614–619.

[9]Hendricks, W. L., "Slip Conditions with Wall Catalysis and Radiation for Multicomponent Nonequilibrium Gas Flow," NASA TMX-64942, 1974.

[10]Moss, J. N., and Bird, G. A., "Direct Simulation of Transitional Flow for Hypersonic Reentry Conditions," AIAA Paper 84-0223, Jan. 1984.

[11]Anderson, D. A., Tannehill, J. C., and Pletcher, R. H., *Computational Fluid Dynamics and Heat Transfer,* McGraw-Hill, New York, 1984, pp. 181–257.

[12]Gordon, R., and Davis, R. T., "An Improved Method for Solving the Viscous Shock Layer Equations," Department of Aerospace Enginering and Engineering Mechanics, Univ. of Cincinnati, Cincinnati, OH, Tech. Rept., Sept. 1985.

[13]Waskiewicz, J. D., Murray, A. L., and Lewis, C. H., "Hypersonic Viscous Shock-Layer Flow Over a Highly Cooled Sphere," *AIAA Journal,* Vol. 16, No. 2, Feb. 1978, pp. 189–192.

[14]Richtmyer, R. D., and Morton, K. W., *Difference Methods for Initial-Value Problems,* Interscience, New York, 1967.

[15]Moss, J. N., "Reacting Viscous-Shock-Layer Solutions with Multicomponent Diffusion and Mass Injection," NASA TR R-411, 1974.

[16]Vigneron, Y. C., Rakich, J. V., and Tannehill, J. C., "Calculation of Supersonic Viscous Flow over Delta Wings with Sharp Supersonic Leading Edges," AIAA Paper 78-1137, July 1978.

[17]Anderson, D. A., Tannehill, J. C., and Pletcher, R. H., *Computational Fluid Mechanics and Heat Transfer,* McGraw-Hill, New York, 1984, pp. 181-257.

[18]Anderson, E. C., and Moss, J. N., "Numerical Solution of the Steady-State Navier-Stokes Equations for Hypersonic Flow About Blunt Axisymmetric Bodies," NASA TM X-71977, June 1974.

[19]Little, H. R., "An Experimental Investigation of Surface Conditions on Hyperboloids and Paraboloids at a Mach Number of 10," M.S. Thesis, Univ. of Tennessee, Knoxville, TN, 1969.

[20]Boylan, D. E., "Laminar Heat Transfer on Sharp and Blunt Ten-Degree Cones in Conical and Parallel Low Density Flow," Arnold Engineering Development Center, Tullahoma, TN, AEDC-TR-73-106, Aug. 1973.

[21]Boyland, D. E., private communication, Sverdrup Technology, Inc., Tullahoma, TN, Feb. 1987.

[22]Jain, A. C., and Adimurthy, V., "Hypersonic Merged Stagnation Shock Layers, Part I: Adiabatic Wall Case," *AIAA Journal,* Vol. 12, No. 3, March 1974, pp. 342-347.

[23]Potter, J. L., and Bailey, A. B., "Pressures in the Stagnation Region of Blunt Bodies in the Viscous Layer to Merged Layer Regimes of Rarefied Flow," Arnold Engineering Development Center, Tullahoma, TN, AEDC-TDR-63-168, 1963.

[24]Bird, G. A., *Molecular Gas Dynamics,* Clarendon Press, Oxford, UK, 1976, pp. 92-96.

Clark H. Lewis
*Associate Editor*